A&A 394, 299–310 (2002)
DOI: 10.1051/0004-6361:20021121

Astronomy & Astrophysics

Flare waves observed in Helium I 10 830 Å

A link between Hα Moreton and EIT waves

B. Vršnak[1], A. Warmuth[2], R. Brajša[1,3,⋆], and A. Hanslmeier[2]

[1] Hvar Observatory, University of Zagreb, Kačićeva 26, 10000 Zagreb, Croatia
e-mail: bvrsnak@geodet.geof.hr
[2] Institute for Geophysics, Astrophysics and Meteorology, University of Graz, Universitätsplatz 5, 8010 Graz, Austria
e-mail: ajw@igam.uni-graz.at
[3] Kiepenheuer-Institut für Sonnenphysik (KIS), Schöneckstr. 6, 79104 Freiburg, Germany
e-mail: rbrajsa@kis.uni-freiburg.de

Received 12 April 2002 / Accepted 29 July 2002

Abstract. Three traveling disturbances recorded in the absorption line of Helium I at 10 830 Å (He I), analogous to Hα Moreton waves, are analyzed. The morphology and kinematics of the wavefronts are described in detail. The He I wave appears as an expanding arc of increased absorption roughly corresponding to the Hα disturbance, although not as sharply defined. He I perturbations consist of a relatively uniform diffuse component and a patchy one that appears as enhanced absorption in He I mottles. It leads the Hα front by some 20 Mm and can be followed to considerably larger distances than in Hα observations. Behind the front stationary areas of reduced He I absorption develop, resembling EUV coronal dimming. The observed He I as well as the Hα disturbances show a deceleration of the order of 100–1000 m s^{-2}. Moreover, in the event where Hα, He I, and EUV wavefronts are observed, all of them follow closely related kinematical curves, indicating that they are a consequence of a common disturbance. The analysis of spatial perturbation profiles indicates that He I disturbances consist of a forerunner and a main dip, the latter being cospatial with the Hα disturbance. The properties and behavior of the wavefronts can be comprehended as a consequence of a fast-mode MHD coronal shock whose front is weakly inclined to the solar surface. The Hα disturbance and the main He I dip are a consequence of the pressure jump in the corona behind the shock front. The He I forerunner might be caused by thermal conduction from the oblique shock segments ahead of the shock-chromosphere intersection, or by electron beams accelerated in the quasi-perpendicular section of the shock.

Key words. shock waves – Sun: flares – Sun: corona – Sun: chromosphere

1. Introduction

Explosive processes in the solar atmosphere, like flares or various forms of fast ejecta, are capable of creating large-scale, large-amplitude MHD disturbances sweeping through the corona (Vršnak & Lulić 2000a, 2000b). Frequently these perturbations steepen into shock waves as revealed by type II radio bursts (cf. Nelson & Melrose 1985). Sometimes a "ground trace" of a coronal disturbance is seen in the chromosphere as the so-called Moreton wave propagating outwards from the flare site (Moreton & Ramsey 1960). These waves are often accompanied by type II bursts, indicating that both phenomena are caused by a common disturbance, most probably a fast-mode MHD shock ignited by the flare (Uchida 1968; Uchida et al. 1973; Uchida 1974).

Recently, the subject was actualized again after the discovery of the so-called coronal EIT waves (Thompson et al. 1998, 1999) observed by the Extreme Ultraviolet Imaging Telescope (EIT) aboard the Solar and Heliospheric Observatory (*SOHO*). Probably the most important result of current research was the simultaneous observation of a Moreton wave, an EIT wave, an associated signature in soft X-rays, and a type II burst (Khan & Aurass 2002). The observations show that all four features are cospatial, i.e. for the first time the coronal and chromospheric signatures were directly related (see also Narukage et al. 2002).

Yet, the discovery of EIT waves introduced also an apparently large disharmony in the overall picture: the Moreton waves and type II bursts often show speeds of about 1000 km s^{-1} (Smith & Harvey 1971) whereas the measured EIT wave velocities turned out to be several times lower (Klassen et al. 2000; see also Eto et al. 2002). The discrepancy was resolved by Warmuth et al. (2001, 2002) who revealed a deceleration of Moreton waves, typically being in the range of several

Send offprint requests to: B. Vršnak,
e-mail: bvrsnak@geodet.geof.hr
⋆ Alexander von Humboldt Research Fellow at KIS.

hundreds m s^{-2}. Since EIT waves are observed only at a low cadence (≈15 min), and since they can be followed to much larger distances than their Hα counterpart, their average velocities (based often on only two measurements) in fact have to be considerably lower. Moreover, since at larger distances the velocity is lower, it can be concluded that EIT waves can be detected even if being of a low fast-magnetosonic Mach number $M_{\rm fms}$, presumably close to 1, unlike the Moreton waves which are observed only if the Mach number is larger than, say, $M_{\rm fms} = 2$ (Warmuth et al. 2001). So, a fraction of coronal perturbations, having low Mach numbers (i.e. the slow ones), might be observed just as EIT waves without any Hα counterpart, additionally increasing the statistical "speed discrepancy".

Although the relationship between the chromospheric Hα and the coronal EUV disturbances is revealed by kinematics, and the deceleration of the blast-shock is comprehended theoretically (see, e.g., Landau & Lifshitz 1987), it would be desirable to strengthen the chromospheric/coronal relationship by observations of the chromospheric signature at distances larger than provided by Hα observations.

Regarding additional chromospheric data, the Helium I absorption line at 10 830 Å (hereinafter He I) has proved to be especially suitable on several grounds. Most obvious is the simple fact that a number of flare waves have been identified in the He I filtergrams which are routinely obtained at the Mauna Loa Solar Observatory (MLSO). Due to the complex line-formation mechanism (described briefly in Sect. 2), the patterns seen in He I images are affected by processes in the chromosphere, transition region, and low corona. In addition, a preliminary inspection of the He I data revealed that He I waves can be traced to considerably larger distances than Hα waves, and could therefore provide a better insight into the relationship between the chromospheric and coronal wave signatures. The results presented below show that He I waves are not only interesting as a "missing link" between Hα and EIT waves but that they also provide a new insight into the nature of the coronal perturbation itself.

We have selected three He I flare wave events: 25 July 1997, 24 August 1998, and 25 November 2000 (an overview is presented in Figs. 1–4) in which a reliable quantitative analysis is possible from the MLSO data. We focus on the morphological aspects and kinematics of the wavefronts in the He I, Hα, and EUV spectral regimes. After giving some basic information on the He I line (Sect. 2), we describe the observations and data reduction techniques in Sect. 3. The basic properties of the analyzed flare waves, their kinematics and perturbation profile evolution, are presented in Sect. 4. The results are interpreted and discussed in Sect. 5 and conclusions are drawn in Sect. 6.

2. The He I 10 830 Å absorption line

The Helium I line at 10 830 Å is formed by electron transitions between the two lowest energy levels of the triplet states of the Helium atom (orthohelium). Since the transitions from triplet states to singlet states (parahelium) are forbidden, the lowest state of the triplet is metastable, acting as a "ground level" of orthohelium. So an electron must be in the lowest triplet state in order to have He I absorption.

The lowest state of orthohelium can be populated in two ways. The first is photoionization by UV and EUV radiation from the corona and subsequent cascading back, called the PR mechanism (photoionization-recombination). The other possibility is the direct excitation by collisions from the ground state of parahelium. The PR mechanism is effective only in regions with temperatures $T < 10\,000$ K, whereas collisional excitation becomes important at $T > 20\,000$ K (Andretta & Jones 1997).

This implies that there are two different height ranges essential for the He I absorption line formation: the upper chromosphere (2000–2400 km above the photosphere) where the PR mechanism dominates, and the transition region (TR) where collisions play the major role. Another important aspect is the structure of the atmosphere, e.g., regions with stronger magnetic fields (plage-like atmosphere) are less sensitive to coronal illumination than the "quiet" regions (Andretta & Jones 1997).

Due to the complex mechanisms involved in the formation of the spectral line, He I filtergrams actually contain information about the upper chromosphere, transition layer, and the low corona. The He I line is usually seen in absorption, except under some special conditions, e.g., in flares. The absorption is reduced (with respect to the quiet sun) in filament channels, but is strong in filaments. Absorption is also increased in ARs and plages, and reduced in coronal holes (Brajša et al. 1996). The quiet Sun is characterized by a weak background and darker patches which reproduce the Hα network (He I mottles; see Giovanelli et al. 1976). A general morphology of solar features observed in He I can be found in, e.g., Brajša et al. (1996).

The He I line is optically thin and various processes can affect its appearance significantly. For example, an increase of the temperature and density in the transition region would enhance the collisional processes, which can bring more atoms to the lowest energy state of the triplet. On the other hand, a temperature/density increase in the low corona would increase its UV radiation output and consequently would provoke an enhanced absorption in the upper chromosphere. At the same time, an increase of the chromospheric density can decrease the effects of the PR mechanism and according to Andretta & Jones (1997) the absorption might be reduced. Bearing in mind also a different response of regions with different atmospheres, and the broad variety of dynamical processes taking place in the solar corona, a number of possibilities should be taken into account when interpreting the He I absorption and its changes.

3. Observations and measurements

3.1. Data sources

He I filtergrams were recorded by the CHIP instrument (Chromospheric Helium I Imaging Photometer; see MacQueen et al. 1998) at the Mauna Loa Solar observatory (MLSO). CHIP uses a liquid crystal variable retarder Lyot filter with a bandpass of 1.4 Å and provides full-disk images at a spatial resolution of 2.″3 pixel^{-1} and a temporal cadence of 3 min.

In addition, we use Hα full-disk images which were obtained at the Big Bear Solar Observatory (BBSO) and which have a spatial resolution of 1.″1 pixel^{-1} and a cadence of 0.5–1 min (see Denker et al. 1999).

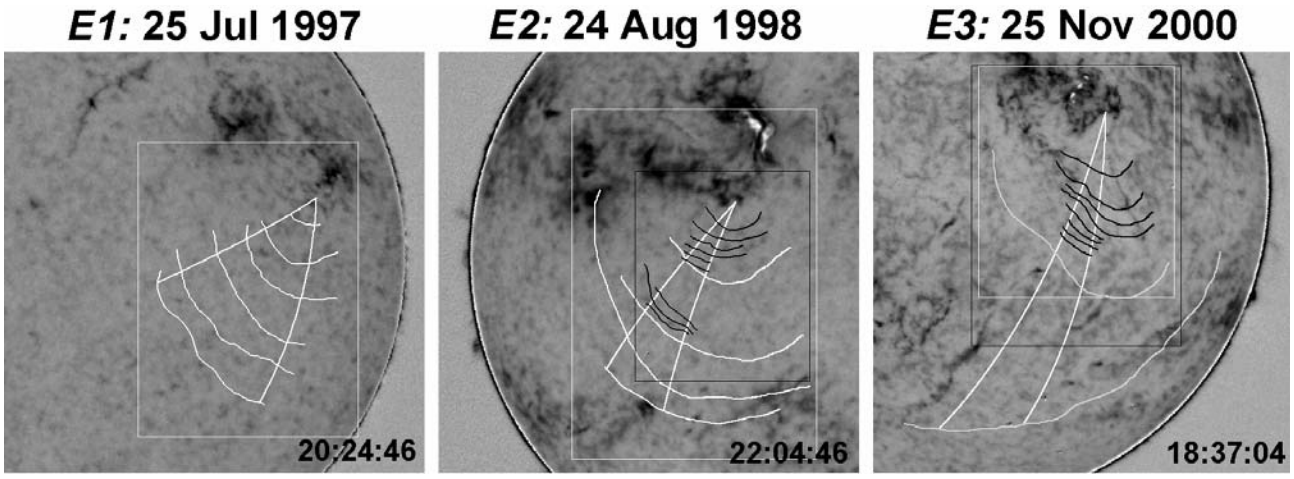

Fig. 1. Subimages of full-disk He I filtergrams from the time of the wave onset for the events of 25 July 1997 (E1), 24 August 1998 (E2) and 25 November 2000 (E3). The visually determined He I, Hα, and EIT wavefronts are drawn by white, black, and gray lines, respectively, together with parts of great circles (white). The white boxes in E1, E2 and E3 are the fields of view of Figs. 2, 3, and 4, respectively. The black black box in E2 gives the field of view for Fig. 6, while the black box in E3 defines the field of view of Fig. 8. In all images, solar north is up, west is right. All times are given in UT.

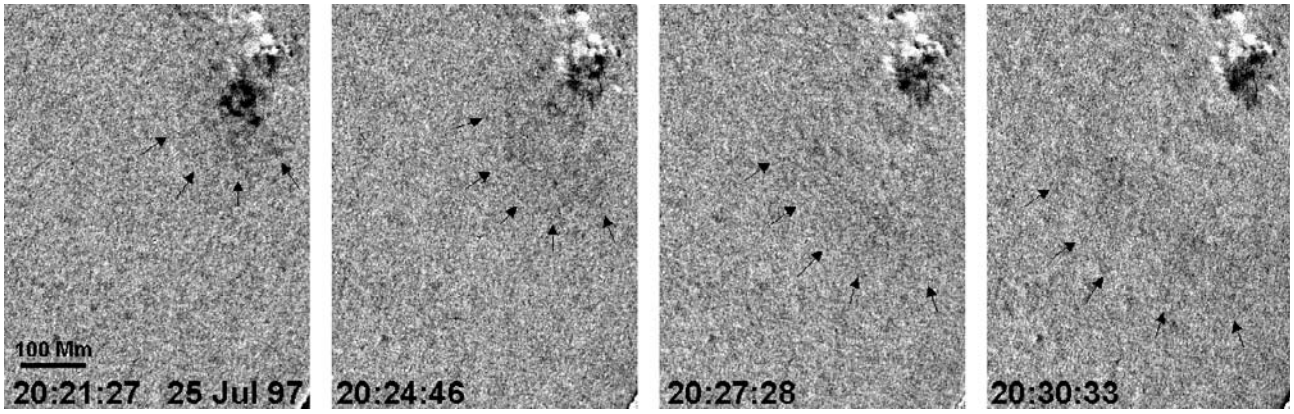

Fig. 2. The He I wave of 25 July 1997 (E1). Difference images are shown, from which a base image from before the event (20:12:45 UT) has been subtracted. The He I wave is seen as a diffuse, expanding dark front, its leading edge is indicated by black arrows. The bright patches in the upper right corner represent the associated flare.

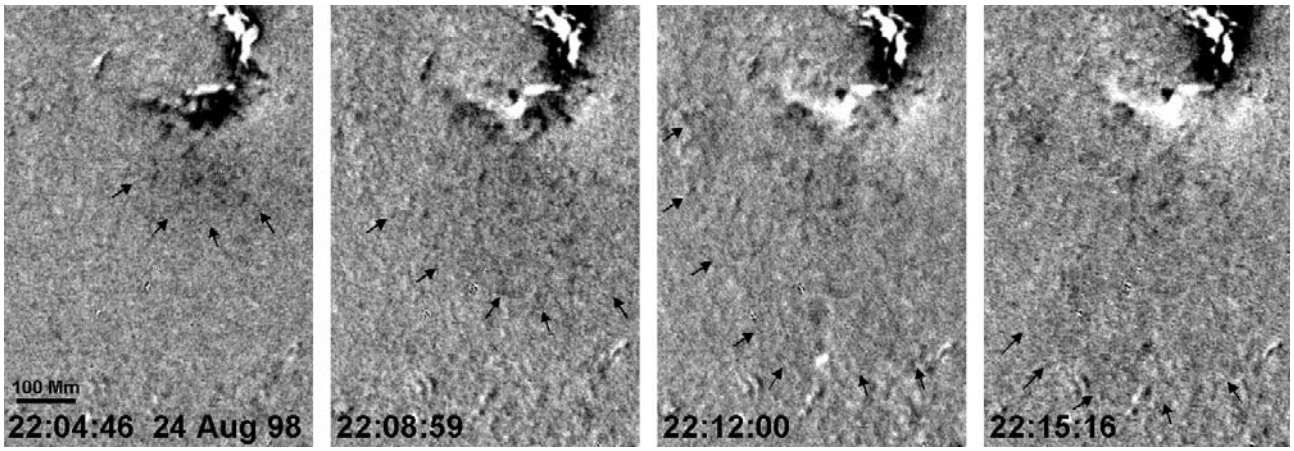

Fig. 3. Difference images revealing the He I wave of 24 August 1998 (E2). The base image was taken at 21:52:50 UT. The vertically oriented bright ribbons in the upper right edge correspond to the main part of the Hα flare, whereas the bright horizontally oriented patches below the ribbons are co-spatial with prominent remote brightenings of the Hα flare. The He I wave seems to emanate from this region.

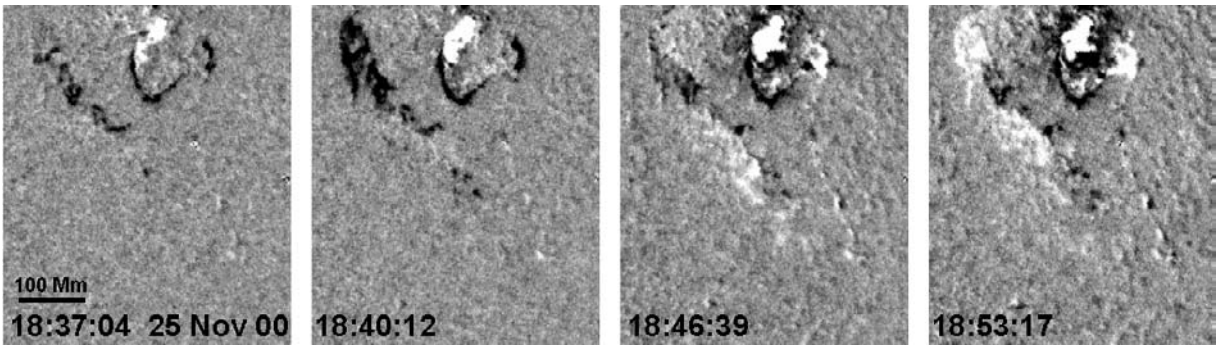

Fig. 4. The He I difference images at the time of the wave of 25 November 2000 (E3). The base image was taken at 18:30:41 UT. The bright patch in the upper middle is the associated flare, the semicircular dark features south of it were secondary brightenings in Hα, which had temporarily the appearance of a third flare ribbon. This was a complex event, with very strong increases and decreases of He I absorption (the dark and light features on the left). The very weak features of the He I wave itself can be seen only in movies, and their kinematics can be obtained only from the intensity profiles.

Coronal imaging data are provided by the Extreme Ultraviolet Imaging Telescope (EIT; Delaboudinière et al. 1995) aboard *SOHO*. In this study, we examine EIT full-disk images at 195 Å (Fe XII; spatial resolution: 2.″6 pixel^{-1}, cadence: ≈15–30 min).

3.2. Data reduction

To study the kinematics and evolution of the flare waves we apply two different methods. The first one is based on the visual identification of the wavefronts using running difference images in which the He I front is dark (increased absorption). The probable starting point of the disturbance is then calculated by fitting a circle to the earliest wavefront, taking the curvature of the solar surface into account. Whereas this method is certainly not exact, it is nevertheless more realistic than arbitrarily adopting that the wave probably originates from the flare center. Moreover, even the presumption that the flare is necessarily the wave source is avoided. Then, the distances of the wavefronts from the starting point are measured along 10 paths which are parts of great circles on a sphere of 1 $R_\odot$ and which cover a certain sector on the solar sphere (see Fig. 1).

The second method provides information not only on kinematics, but also on the morphological evolution of the wavefronts. Using the same starting point as in our first method, we obtain intensity profiles along a large number of directions (so that each pixel in the measured sector is sampled at least once) which are then averaged laterally over the complete sector angle. In this way we obtain, for a given moment, the mean intensity as a function of distance, averaged over the whole angle into which the wave propagates. From these profiles we measure the locations of some distinct profile elements like, e.g., the leading edge, the intensity maximum, etc.

In Fig. 5 the profile method is illustrated by four successive He I perturbation profiles of the event of 25 July 1997. The profiles are obtained by subtracting the image at the moment τ and the "background" image taken at τ_0 being the last frame without a visible wavefront[1]. The intensity residual at $t = \tau - \tau_0$ is defined as $\Delta I(t) = I(\tau) - I(\tau_0) \equiv I - I_0$, and is expressed in arbitrary units.

The residuals ΔI are plotted as a function of the distance r from the calculated source. The He I wavefront of increased absorption is seen as a dip in the profile. All events show the broadening of the profile ($\partial \Delta r / \partial t > 0$) and decreasing amplitude, just like Hα disturbances do (Warmuth et al. 2001).

3.3. Description of the events

The general data for the three analyzed events are given in Table 1 (note that in the first column we introduce the event labels E1, E2, and E3, which will be used hereinafter). Large-scale He I images are shown in Fig. 1 for an overview. Table 1 includes the basic parameters of the associated flares: in the 2nd–6th column the NOAA active region number, location, Hα/SXR importance, soft X-ray (SXR) burst beginning, and SXR burst maximum, are presented, respectively.

The velocity of a possibly associated coronal mass ejection (CME) is given in the 7th column. In the case of E2, *SOHO* and its LASCO coronagraph (Brueckner et al. 1995) were off-line, and the Mauna Loa Mark III K-coronameter (Fisher et al. 1981) did not observe any coronal activity. However, since this was a disk event, a CME might easily go undetected, and indeed an interplanetary type II radio burst was observed by *Wind*/WAVES (Bougeret et al. 1995), which is a strong indication for the presence of a CME. In E3, the possibly associated CME was a full halo event.

The time of the earliest observed wave signature is given in the 8th column. The number of wavefronts measured (n) is given for each wavelength separately in the 9th, 10th, and 11th column, distinguishing the two methods described in Sect. 3.2 (v – "visual" method, p – "profile" method). Note that E1 was observed only in He I, while we have also Hα data for E2, and E3 has additional coverage in both Hα and EUV.

In all of the analyzed events the flare was located at the periphery of the active region (AR). E2 and E3 both represent impulsive X-class flares, whereas E1 was associated with a mere

[1] In the profile method we are using *differenced images* because due to the large spatial extent of the He I disturbance the trailing part of the perturbation profiles cannot be obtained from *running difference images*.

Table 1. List of events.

label & date	NOAA No.	flare locat.	flare imp.	SXR beg.	SXR max.	CME (km s^{-1})	wave UT>	Hα n_v/n_p	He I n_v/n_p	EIT n_v/n_p
E1: 25 Jul. 1997	8065	N16W54	SF/C4	20:09	20:35	611	20:21.5	-/-	4/4	-/-
E2: 24 Aug. 1998	8307	N35E09	3B/X1	21:50	22:12	?	22:03.2	9/6	4/4	-/-
E3: 25 Nov. 2000	9236	N20W23	2B/X2	18:33	18:44	671	18:39.2	8/6	-/6	2/-

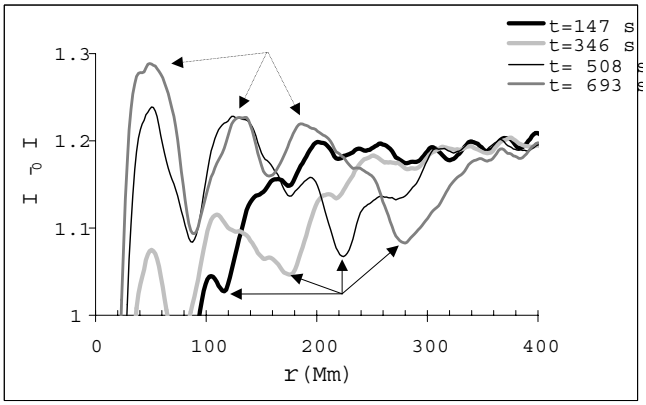

Fig. 5. Profiles of the 25 July 1997 He I wave obtained from difference images. The elapsed times $t = \tau - \tau_0$ are indicated in the legend ($\tau_0 = 20{:}19$ UT). The perturbation dips and regions of post-wave reduced absorption are indicated by arrows.

C4 flare, with an even longer rise time than for the two X-class flares. Yet it showed a clearly visible propagating wavefront in He I, albeit slower and weaker than in E2. In E3, the propagating wavefront in He I was only weakly visible (in contrast to Hα and EUV, which showed nicely developed fronts), but stationary features behind the front were very prominent (discussed in Sect. 5.3). All events were associated with metric type II radio bursts.

4. Results

4.1. Morphology of disturbances

In Fig. 6 (left column), two He I difference images show the development of the flare wave of 24 August 1998 (E2). The He I wave can be seen as an expanding broad arc-shaped front of increased absorption. The dark front is inhomogeneous and lacks a sharp edge. It consists of an extended diffuse component and a number of discrete darker patches. These patches coincide with the He I mottles (see the left and center panels of Fig. 7) that reproduce the chromospheric network in He I. On the other hand, the He I mottles are closely associated with the photospheric magnetic field which is documented by the longitudinal magnetogram shown in the right panel of Fig. 7 (acquired by the NASA/NSO Spectromagnetograph at Kitt Peak National Observatory; Jones et al. 1992). So the patchy features in the wavefront are caused by the increased absorption in the magnetic field concentrations.

For comparison, in the right column of Fig. 6 nearly contemporaneous Hα running difference images of E2 are shown. The Moreton wave is seen as an arc-shaped bright front. Like the He I front, the Moreton front is composed of a diffuse part

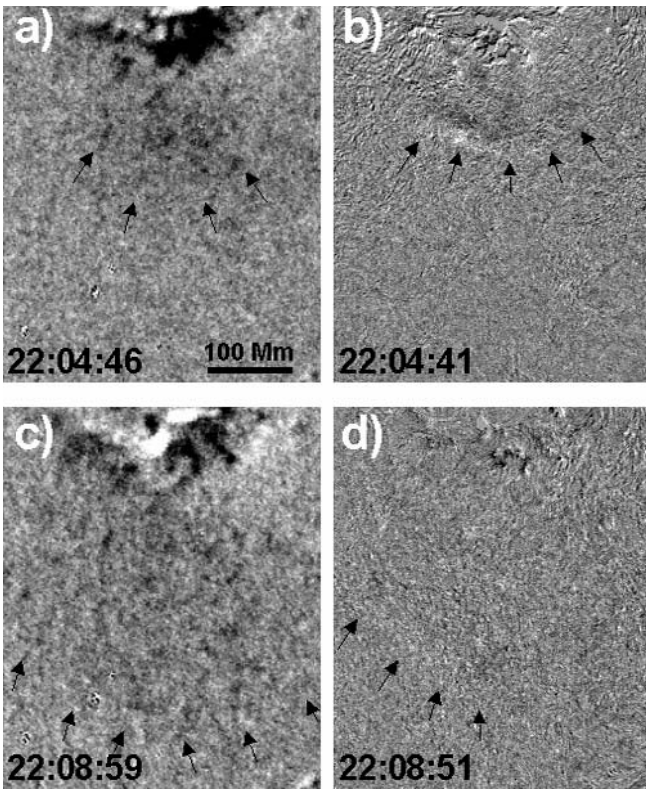

Fig. 6. The development of the flare wave of 24 August 1998 (E2), seen in He I difference images **a), c)** and Hα running difference images **b), d)**. The Hα wave has a much smaller thickness and clearly lags behind the He I wave. The dark front behind the bright Hα wavefront is an artifact of the running difference method.

and some stronger localized brightenings. However, these localized patches are much smaller than those in He I and we were not able to identify them with the network elements.

In Hα, the wavefront has a much better defined leading edge than in He I, and a much smaller width Δr. Just by comparing the He I and the Hα images in Fig. 6 one gets the impression that the He I wave leads the Moreton wave. This will become evident from the kinematical curves which are presented in the following section and discussed in detail in Sects. 5.1 and 5.2.

Hα and He I fronts seem to originate from roughly the same region. In E2, where both wavefronts are defined clearly enough so that they can be used to extrapolate a starting point (see Sect. 3.2), the calculated origins differ by about 20 Mm. We believe this is not an evidence for different origins but rather a sign of the limited accuracy of the extrapolation method.

As in Warmuth et al. (2001), the calculated origins in all three events are lying well in the periphery of the AR.

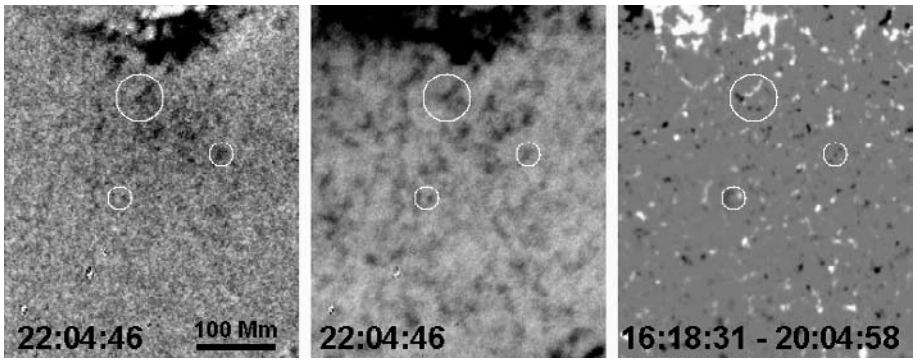

Fig. 7. Association of He I mottles with the photospheric magnetic field in E2. In the left panel, a difference image shows the earliest He I wavefront. A comparison with the direct He I image (center) shows that the darker patches of the He I wavefront coincide with the He I mottles which in turn are closely associated with the photospheric magnetic field (right; the two times given in the magnetogram correspond to the begin and end of the scan).

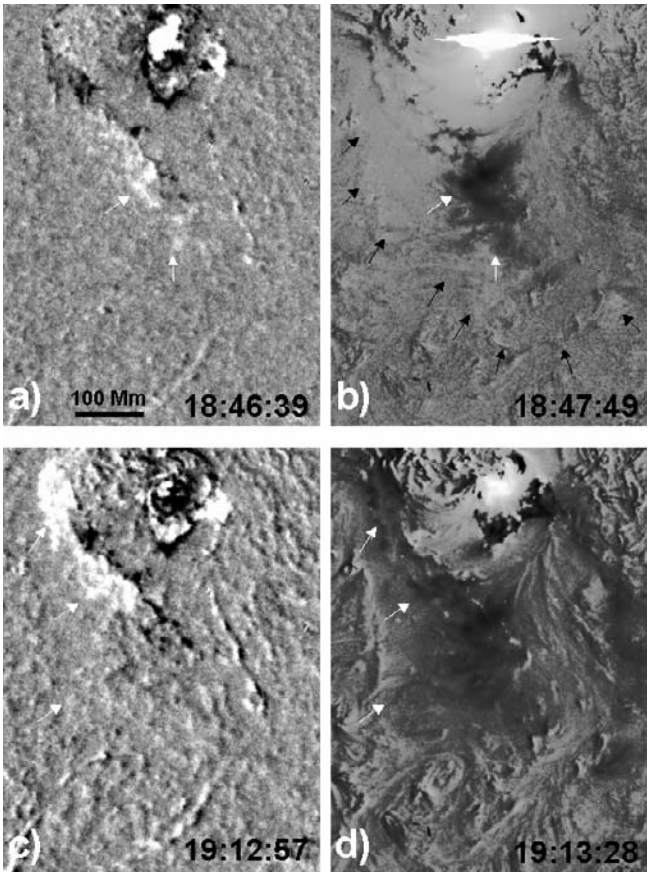

Fig. 8. Development of He I brightening **a), c)** and EIT dimming **b), d)** as shown by difference images of E3. Where the EIT dimming is strong, the He I absorption tends to be reduced (some of these features are indicated by the white arrows), although there is no one-to-one correspondence. In addition, image **b)** shows the first EIT wavefront (black arrows).

Moreover, they are even not located within the main flaring region but rather at its periphery or in some of the secondary brightenings in the outskirts of the flare.

Some regions behind the dark He I front show a weakening of absorption (white in difference images), morphologically similar to the coronal dimming usually observed behind EIT waves (see, e.g., Thompson et al. 2000). In the upper right corner of Fig. 6c, a region of diffuse reduced absorption can be seen. This area remained at a fairly constant brightness for at least two hours.

Another example of this phenomenon can be seen in Fig. 8, which shows difference images in He I (left) and EUV (right) for E3. The widening EIT dimming area is clearly visible. A comparison with the contemporaneous He I images shows that at the locations where the dimming is strong in EIT, the He I absorption tends to be reduced with respect to the pre-event state, although there is no one-to-one correspondence. The reduced absorption also consists of a diffuse and a discrete patchy component.

4.2. Kinematics

The kinematics of a given wavefront was measured using two procedures, the first one being based on the visual estimate of the leading edges, while in the second method the front was determined using the perturbation profiles. The kinematics was also measured for some other distinct parts of the perturbation profiles specified in Sect. 4.3.

In Figs. 9a–c the distance r of perturbation front is shown as a function of time t for all studied events. The zero-time ($t = 0$) corresponds to the probable starting time of the disturbance. The distances of the leading fronts measured with the "visual" method along ten directions within the sector spanned by the wave (see Sect. 3.2) are averaged and the obtained values $\overline{r}$ are shown in Fig. 9 together with the error bars. The size of the error bars is primarily governed by a non-circular shape of the wavefronts. In the case of the Hα and He I wave fronts it typically amounts to ±5–10 Mm, never exceeding 20 Mm. The distances obtained using the perturbation profiles are shown by squares (He I) and triangles (Hα) whose sizes roughly correspond to the error of the measurements. Here, beside the intrinsic error due to the non-circular shape of the front, an error due to the "noise" in the data becomes important, not allowing the accuracy better than ±10 Mm (see Fig. 5).

Although the two methods show some differences, the results are qualitatively the same. Figures 9b and 9c reveal that the Hα and the He I perturbations are obviously related since

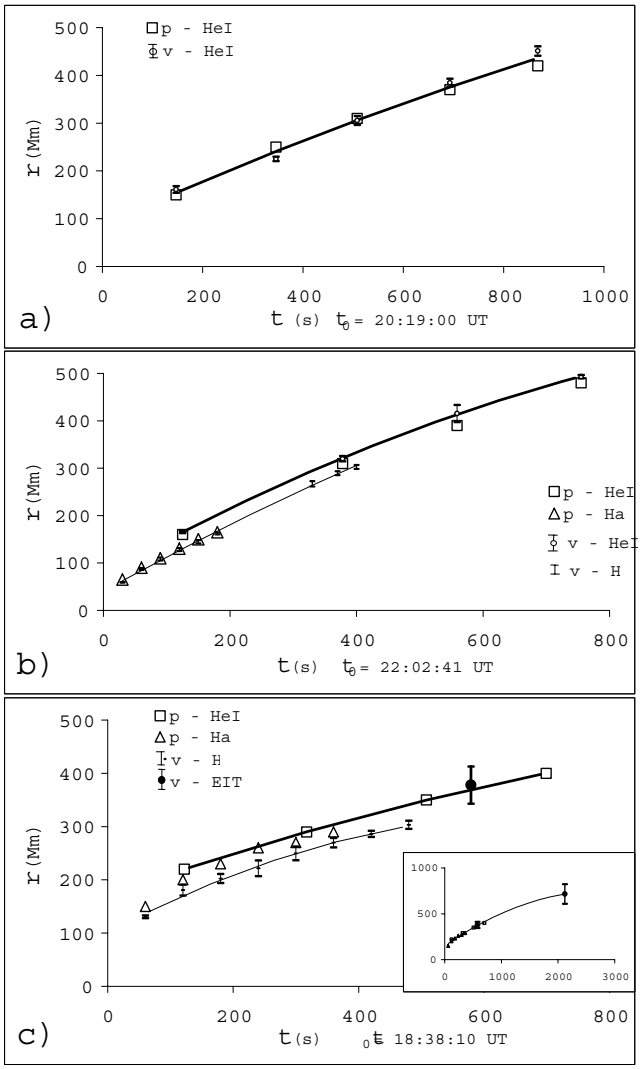

Fig. 9. The kinematics of the leading fronts of the analyzed perturbations: **a)** 25 July 1997 (E1); **b)** 24 August 1998 (E2); **c)** 25 November 2000 (E3). The second degree polynomial least squares fits are shown (bold lines – He I, thin – Hα). The error bars are indicated for the visual method, whereas in the case of the profile method the error is roughly represented by the size of the symbols used. In the inset in the bottom panel the distance range is extended to include the most distant EIT wave signature measured.

they follow closely associated kinematical curves. Yet, the He I fronts are leading the Hα fronts for about 20–40 Mm. The best observed event is E3 with Hα, He I and EUV coverage, and Fig. 9c exposes that all three wave signatures are a consequence of a common disturbance. In this event, the profile method seems to be more sensitive than the visual method in tracing the wavefronts (unlike in the other two events): the He I wavefront was too dim to be determined clearly with the visual method, and in Hα the profile-wavefront was ahead of the visual one. Because of this the distance between the He I-profile wavefront and the Hα-profile wavefront was amounting to ≈20 Mm whereas the distance to the Hα-visual wavefront was ≈40 Mm.

Like in the cases described by Warmuth et al. (2001, 2002), E2 and E3 clearly expose a deceleration regardless of the method applied. In E1, where the wave was observed only in He I, the situation is somewhat less clear. Whereas the profile method shows a deceleration (the second degree polynomial least squares fit gives $\overline{a}_{\rm p} = -399\ {\rm m\,s^{-2}}$), the visual method gives a weak acceleration ($\overline{a}_{\rm v} = +71\ {\rm m\,s^{-2}}$). The fit joining the data obtained by the visual and profile method (with equal statistical weights) shows a deceleration of $\overline{a}^{*} = -167\ {\rm m\,s^{-2}}$ (shown in Fig. 9a, and Table 2).

In Table 2, the basic kinematical parameters of the waves are summarized. The average velocities $\overline{v}$ are obtained using a linear least-squares fit, whereas the average accelerations $\overline{a}$ and the velocities at the time of the first observed wavefront (v_1) are calculated from the fitted second degree polynomials. We note that the obtained values do not depend on the choice of the initial time and the wave source position. Most of the values in Table 2 are based on the visual method since it seems to be more accurate usually. As already mentioned, in E1 the values are obtained by joining the visual and the profile method. For E3, the He I values (in brackets) are obtained using the profile method since the wavefront was too diffuse and weak to be defined reliably enough by the visual method. Furthermore, for E3 the average acceleration $\overline{a}_{\rm comb}$ obtained using the He I-profile, Hα-profile, and EIT-visual data is shown (the fit is drawn in the inset of Fig. 9c). In the last three columns the largest distance $r^{\rm max}$ at which the wavefront at a given wavelength could still be reliably identified is given in Mm (10^6 m).

Inspecting Table 2 one finds that the tabulated Hα velocities are larger than those of the He I wavefronts. This is primarily caused by the different time intervals in which the two perturbations were observed. Due to the lower cadence of the He I observations the Hα perturbation is usually observed earlier. Since the propagation speed of wavefronts is decreasing in time, the He I fronts show lower v_1 and $\overline{v}$. Yet, at the same instant t the velocities are approximately equal (see in Figs. 9b and c the intervals $200 < t < 400$ s). So although the He I perturbation is ahead of the Hα front, through the period covered by simultaneous observations they have similar velocities. Such a behaviour will be discussed in Sects. 5.1 and 5.2.

4.3. Perturbation profile evolution

Perturbation profiles (Sect. 3.2) were determined in all three events. In E2 and E3, which both had well defined He I and Hα perturbation profiles, we followed the kinematics of the beginning (b), maximum (m), and end (e) of the perturbations. The results are presented in Fig. 10. As already seen in Figs. 9a and 9b He $I_{\rm b}$ is ahead of H$\alpha_{\rm b}$. H$\alpha_{\rm m}$ shows a tendency to be cospatial with He $I_{\rm m}$.

Finally we analyze in detail the co-temporal He I and Hα profiles. The only three available cases are shown in Fig. 11. Each profile is obtained as the intensity difference between the actual profile and the previous one (equivalent to measuring the profile from a running difference image). Thus, only the leading parts of the profiles are reliable since the previous profile

Table 2. Kinematics of Hα, He I, and EIT wave fronts (denoted by respective subscripts); v_1 – velocity at the time of the first observed wavefront; $\overline{v}$ – average velocity; $\overline{a}$ – average acceleration; $\overline{a}_{\rm comb}$ – average acceleration evaluated in E3 merging the Hα, He I, and EIT data sets; $r^{\rm max}$ – the largest distance at which the perturbation was observed. The values in brackets are based on the profile method.

label & date	$v_{1\,\mathrm{H}\alpha}$ km s^{-1}	$v_{1\,\mathrm{He\,I}}$ km s^{-1}	$\overline{v}_{\mathrm{H}\alpha}$ km s^{-1}	$\overline{v}_{\mathrm{He\,I}}$ km s^{-1}	$\overline{v}_{\rm EIT}$ km s^{-1}	$\overline{a}_{\mathrm{H}\alpha}$ m s^{-2}	$\overline{a}_{\mathrm{He\,I}}$ m s^{-2}	$\overline{a}_{\rm comb}$ m s^{-2}	$r^{\rm max}_{\mathrm{H}\alpha}$ Mm	$r^{\rm max}_{\mathrm{He\,I}}$ Mm	$r^{\rm max}_{\rm EIT}$ Mm
E1: 25 Jul. 1997	-	451*	-	391*	-	-	–167*	-	-	450	-
E2: 24 Aug. 1998	946	610	655	524	-	–382	–514	-	300	500	-
E3: 25 Nov. 2000	836	(385)	390	(320)	285	–885	(–185)	(–156)	300	400	800

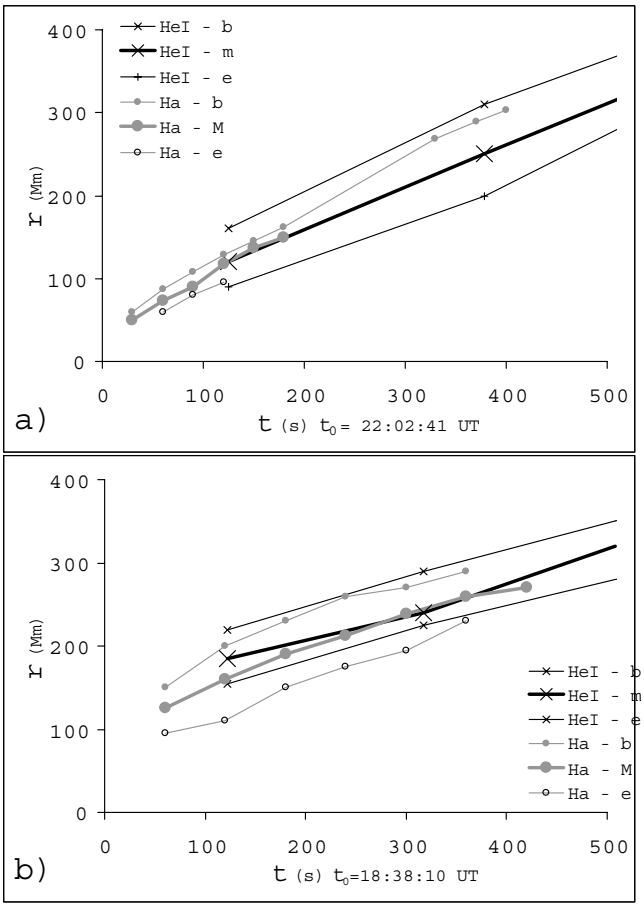

Fig. 10. The kinematics of different parts of the perturbation profiles: **a)** 24 August 1998 (E2); **b)** 25 November 2000 (E3).

provides information on the unperturbed background only ahead of the disturbance.

The profiles in Fig. 11 again show that the frontal edge of the He I profiles is leading in front of the beginning of Hα profiles. However, Fig. 11 reveals a new important aspect of the He I profiles: the leading edge of the He I profile shows a two-step shape. This is clearly exposed in Fig. 11, but we note that almost all He I perturbation profiles show such a behavior (with or without applying the "background subtraction"). Figure 5 can be taken as an example where the first (shallow) step segments are located at r = 140–150 Mm, r = 210–250 Mm, r = 260–310 Mm, and r = 340–370 Mm, for the times t = 147 s (bold), t = 346 s (thick-gray), t = 508 s (thin), and t = 693 s (thin-gray), respectively.

Figure 11 reveals that the beginning of the the second (deeper) step corresponds to the beginning of the Hα perturbation. Because of this we will call the shallow frontal segment of the He I perturbation the "He I forerunner".

5. Interpretation

In the following we propose an *ad hoc* interpretation of the observations. Since the formation of the He I 10 830 Å line is quite complex (see Sect. 2), details regarding the line formation are beyond the scope of the following interpretation.

The geometry of the disturbance is proposed in Fig. 12. Since the coronal fast magnetosonic speed increases with height (Mann et al. 1999), the fast-mode MHD shock front at low heights is weakly inclined to the magnetic field lines and is curved (see, e.g., Uchida et al. 1973; Wu et al. 2001)[2].

5.1. The main perturbation dip

We suppose that the Hα perturbation (Moreton wave) is caused by a sudden pressure jump in the corona when the shock front surpasses a given point in the chromosphere (denoted as r = 2 in Fig. 12)[3]. The plasma is pushed down, but due to inertia it takes some time to get maximum compression. In this period of downward plasma motion the Moreton wave is seen in absorption in the red wing of the Hα line and in emission in the blue wing (Dodson & Hedeman 1968). In the line center, the maximum ΔI in Hα is reached (r = 3 in Fig. 12) when the downward motion stops, i.e. before the chromosphere starts to "relax".

The pressure jump behind the shock causes a density/temperature increase not only in the chromosphere but in the transition region as well. The collisional processes are enhanced, leading to an increase in the population of the ground level of ortohelium which increases the absorption in He I. The segment of the perturbation created in this way is cospatial with the Hα disturbance.

[2] Such an inclined shock geometry is observed at low heights in EIT and SXT waves observed above the limb, e.g. in the event of 6 May 1998 presented by H. Hudson at the CESRA Workshop on Energy Conversion and Particle Acceleration in the Solar Corona held at Ringberg Castle, Tegernsee/Munich, 2–6 July 2001.

[3] We note that the disturbance is never observed in the closest vicinity of the flare. This can be explained by the time/distance needed to create a shock from the blast (Vršnak & Lulić 2000a). Before the shock formation the chromospheric plasma adjusts to a gradual coronal pressure increase through a series of quasi-equilibrium states, i.e. there are no abrupt plasma motions.

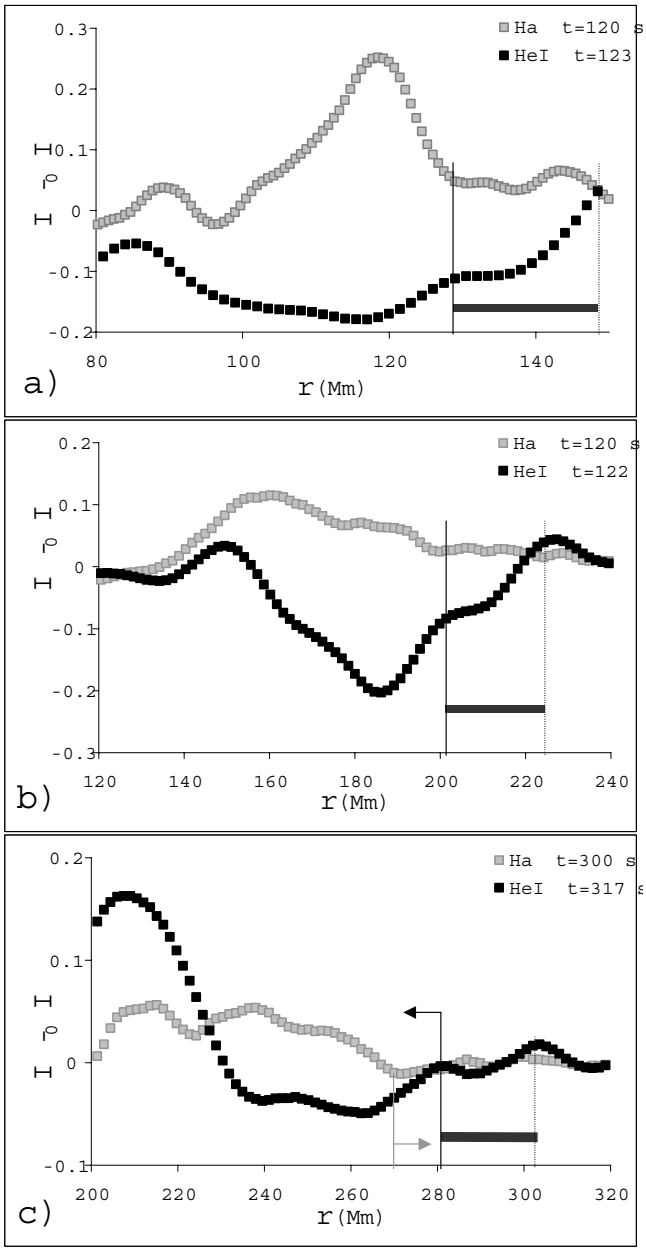

Fig. 11. The co-temporal Hα and He I perturbation profiles: **a)** 24 August 1998 (E2) at t = 120 s after τ_0 = 22:02:41 UT; **b)** 25 November 2000 (E3) at t = 120 s after τ_0 = 18:38:10 UT; **c)** 25 November 2000 at $t \approx 300$ s. The He I "forerunner" is indicated by the bold horizontal line. In the bottom panel the horizontal black arrow approximately indicates for how far the He I profile should be shifted backwards in order to compensate the 17 s time difference between the moments at which Hα and He I profiles were measured (the gray arrow indicates the corresponding forward shift of the Hα profile).

An additional contribution can come from the PR mechanism in the upper chromosphere due to the enhanced UV radiation from the low corona (evidenced by the EIT wave). Since the PR mechanism is less effective in a plage-like atmosphere (Andretta & Jones 1997), and since it is caused by a comparatively uniform UV illumination from the corona, it can be considered as the cause of the diffuse component of the perturbation.

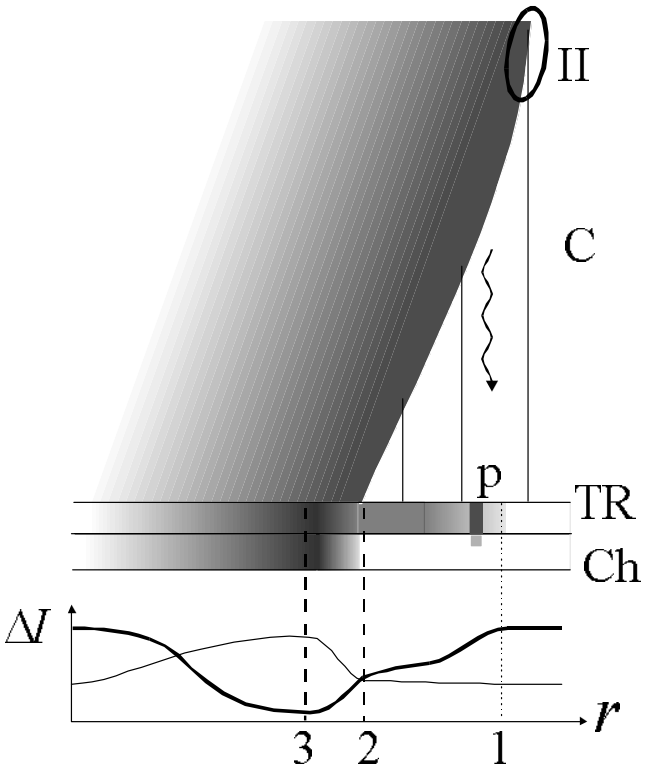

Fig. 12. Schematic presentation of the fast-mode MHD shock passage through the corona (C) and its signatures in the transition region (TR) and chromosphere (Ch). Thin vertical lines represent magnetic field lines and the wavy arrow indicates the agent causing the He I forerunner. The shading behind the shock front above the TR illustrates the density and temperature enhancement in the shock downstream region. The type II burst source is indicated (II) in the quasi-perpendicular segment of the shock. At the bottom, the He I and Hα intensity profiles are represented by the bold and thin line, respectively.

5.2. The forerunner

Adopting that the Hα disturbance and the main He I dip are created in the region behind the intersection of the shock front and the coronal base (r = 2 in Fig. 12), the He I forerunner indicates that the population of the lowest state of orthohelium in the transition region and/or chromospheric plasma is increased already before the shock arrival (the $2 > r > 1$ region in Fig. 12). Again, the increased coronal UV emission from the shocked coronal plasma above causes only the diffuse component of forerunner.

The patchy component is associated with the magnetic field concentrations (Fig. 7). In the following, we stress two feasible processes, involving different agents, which can account for the forerunner (indicated schematically by the wavy arrow in Fig. 12, where "p" symbolizes a patchy element of increased absorption).

In an oblique MHD shock, the thermal conduction can carry out the heat along the magnetic field lines into the

upstream region. In particular, the heat can be transported downwards from the lower segment of the shock where the angle between the shock and the magnetic field lines is comparatively large (Fig. 12). In this way, the transition region can be excited ahead of the intersection point ($2 > r > 1$ in Fig. 12).

In fact, due to the large temperature gradient at the shock front, the thermal conduction is saturated and a thermal conduction front is created in the upstream region. The conductive energy flux can be estimated to about $\Phi \approx n_e k_B T_e (k_B T_e/m_e)^{1/2}/4$ (Manheimer & Klein 1975, see also McDonald et al. 1999 and references therein), where k_B, T_e, and m_e are the Boltzman constant, electron temperature, and the electron mass, respectively. When the conduction front, moving downwards along the magnetic field at the speed $v_{th} \approx \sqrt{k_B T_e/m_e}$ reaches the transition layer, the temperature increase causes an enhanced electron excitation, populating the lowest state of orthohelium and increasing the absorption.

On the other hand, bearing in mind the quasi-perpendicular nature of the shock one more process becomes feasible. In the upstream region electrons can be accelerated (see, e.g. Benz 1993) and those directed downwards (see, e.g., Stewart & Magun 1980) can themselves collisionally increase the population of the lowest state of orthohelium in the transition region. Moreover, the precipitating non-thermal electrons rise the plasma temperature which can additionally enhance the collisional effects.

To check these possibilities we evaluate some of the relevant physical quantities. The velocities of the disturbances at distances where the He I wave is observed are about $v \approx 400$–$600\ \mathrm{km\,s^{-1}}$ (see Table 2). Using for the fast magnetosonic speed at low heights $v_{fms} \approx 200$–$300\ \mathrm{km\,s^{-1}}$ (Mann et al. 1999; Wu et al. 2001), one can estimate the fast-magnetosonic Mach number of the shock to $M_{fms} = v/v_{fms} \approx 2$ (for details see Warmuth et al. 2001). Shocks having such a Mach number are strong enough to provide the electron acceleration and create electron beams (Mann et al. 1994; see also Mann et al. 1999).

For the perpendicular shock the ratios of the downstream to upstream densities ($X_{21} = n_2/n_1$), pressures ($P_{21} = p_2/p_1$), and temperatures ($T_{21} = T_2/T_1$) are related to M_{fms} as:

$$M_{fms}^2 = \frac{X(X+5+5\beta)}{(4-X)(2+5\beta/3)}, \quad (1)$$

$$P_{21} = 1 + M_{fms}^2 \left(\frac{2}{\beta} + \frac{5}{3}\right)\left(1 - \frac{1}{X_{21}}\right) - \frac{1}{\beta}\left(X_{21}^2 - 1\right), \quad (2)$$

and

$$T_{21} = P_{21}/X_{21}, \quad (3)$$

respectively, where $\beta = 2\mu p/B^2$ is the gas to magnetic pressure ratio in the upstream region, and the heat capacity ratio $\gamma = 5/3$ was used. For a $\beta = 0.1$–1 (Gary 2001; Wang 2000, and references therein) and $M_{fms} = 2$ one finds $X_{21} = 2.13$–2.18[4].

[4] This is compatible with the observed emission band-split in the associated type II bursts. The relative split defined as $BDW = (f_2 - f_1)/f_1$, where f_1 and f_2 are the emission frequencies of the split band (Vršnak et al. 2001), amounted to $BDW = 0.5$ and $BDW = 0.45$ for E1 and E2, respectively. Since $f^2 \propto n$, the band-split is associated with the density jump at the shock front as $X_{21} = (1 + BDW)^2$ (Vršnak et al. 2001) and one finds $X_{21} = 2.25$ and 2.10, respectively.

Using Eqs. (2) and (3) one finds $T_{21} = 5.51$–2.36, i.e. $T_2 \approx 4$–10×10^6 K for $T_1 = 2 \times 10^6$ K. This gives for the speed of the thermal conduction front $v_{th} \approx 2500$–$4000\ \mathrm{km\,s^{-1}}$. Using $n_e = 10^8$–$10^9\ \mathrm{cm^{-3}}$ for the coronal electron density one finds that the thermal conduction flux can not be larger than, say, $\Phi = 4 \times 10^5\ \mathrm{W\,m^{-2}}$, which is at least one order of magnitude lower value than found in flares (e.g. Rust & Somov 1984). The conduction front can be formed only if v_{th}, which is directed along the field lines (i.e. normal to the solar surface), is larger than the shock speed component perpendicular to the magnetic field lines (the horizontal speed v_{sh}). Denoting the angle between the shock front and the vertical as θ one finds the condition $\tan\theta > v_{sh}/v_{th}$. Using the obtained values for v_{th} and the measured values $v_{sh} = 400$–$600\ \mathrm{km\,s^{-1}}$ one finds $\theta > 15^o$, showing that already at small shock inclinations the thermal conduction can become effective.

Finally, we note that the distance between the He I forerunner and the Hα front does not change significantly over the distance of some 100 Mm (see in Figs. 9b and 9c the kinematical curves between $t \approx 200$ s and $t \approx 400$ s). Such a characteristic obviously contains important information about the shock evolution. However, the 3-D problem of the MHD shock propagation, in a magnetoplasma changing with the height above the surface where the field lines are anchored is extremely complex and at this point we can only speculate about a possible explanation for the described behaviour.

Before considering other options, we stress that the accuracy of measurements is comparatively low and we are not allowed to state that the velocities of the Hα front and He I forerunner in the considered range of distance are really the same. Furthermore, as the perturbation weakens, it is increasingly difficult to estimate the real extent of the forerunner (see e.g. Fig. 5), so its velocity might be underestimated.

If, on the other hand, the velocities of the Hα front and He I forerunner are really equal in the considered range of distances, two important circumstances should be kept in mind. The first one is that the Alfvén velocity in the vicinity of an active region changes with the height, as well as with the lateral distance, and attains a minimum at a certain height/distance range (Mann et al. 1999, 2002; see also Wu et al. 2001). So it is possible that the shock front geometry (the inclination) becomes "stable" after the shock formation is completed.

The other important point is that the shock amplitude is decreasing with distance. This means that the temperature excess in the downstream shock region is decreasing, governing also the velocity of the thermal conduction front. In such a situation when both the shock front and the thermal conduction front are slowing down, a possible outcome is an approximately constant distance between the forerunner and the main perturbation, the former covering the area behind the conduction front, and the latter the region behind the shock front.

5.3. Coronal dimming

Coronal dimming is often observed between a flare and an EIT wave, lasting for up to several hours. It is interpreted as

a depletion of coronal material, but the underlying process has not been identified yet (Thompson et al. 2000).

The diffuse part of the reduced He I absorption thus may be associated with the decreased illumination from the depleted low corona behind the EIT front. However, the correspondence between EIT and He I features is not necessarily exact (see Fig. 8). Moreover, some of the areas of reduced He I absorption are quite sharply defined, especially in E3. So, some other physical processes, presumably a variation of conditions in the transition region (Andretta & Jones 1997), may be at least equally important in this case.

In E2, a diffuse reduced absorption observed in the SW part of the AR (see Fig. 6) could really be due to coronal dimming. The area remained at a fairly constant brightness for at least two hours, which is comparable to the dimming usually observed in the EUV. This brightening is not visible in the intensity profiles discussed in the previous section, since it does not overlap with the measured area.

In E1, the weakest event, only some small-scale brightenings in the immediate vicinity of the flare can be found. These brightenings are clearly recognizable in the perturbation profiles shown in Fig. 5 (indicated by arrows at the locations r = 50, 130, and 190 Mm).

Finally we note that the events E1 and E3, and most probably also E2, were associated with CMEs. So the coronal depletion could be caused by the expansion of the erupting volume and/or its interaction with the ambient magnetic fields. Such a process can cause "opening" of field lines leading to the formation of transient coronal holes (see, e.g., Manoharan et al. 1996; Vršnak et al. 2002). These could be the regions where EUV dimming and He I reduced absorption overlap. Yet, it should be emphasized that in such a case the EUV dimming, respectively the He I brightening, are probably not directly related with the wave phenomenon. Inspecting the kinematical curves of the CMEs that were associated with E1 and E3, one finds that at the time of the first wavefront appearance, the CME leading edges had already reached the projected height of about two solar radii. It is not likely that such a large scale phenomenon could drive the disturbances which reached the distance of only 100–200 Mm, i.e. which are of almost ten times smaller scale.

6. Conclusion

The results presented in Sect. 4 show that the observed Hα, He I, and EIT waves are consequences of a common disturbance that is associated with the flare. In all events, the flares are located in the periphery of the AR, and the source region of the disturbance is in the outskirts of the flaring region. The perturbation speed at the time of the first appearance of the wavefront is close to 1000 km s^{-1}. This is 2–3 times faster than the expected coronal fast magnetosonic speed outside active regions. The disturbance decelerates, which is accompanied by perturbation broadening and an amplitude decrease. The events are associated with metric type II radio bursts. All this indicates that the Hα – He I – EIT disturbance can be interpreted in terms of a fast-mode MHD shock wave formed from a large amplitude perturbation ("simple wave"), ignited most likely by the flare[5].

In He I, the disturbance can be followed to considerably larger distances than in Hα, thus providing a link to EIT waves. Morphologically the He I wave is more similar to the EIT wave: It has a broader profile than the Hα wave and a feature resembling coronal dimming can appear behind the wavefront.

An important characteristic of the He I perturbation profile is the He I forerunner ahead of the Hα perturbation front and the main He I dip. This feature most probably reveals a communication between higher parts of the inclined shock front and the surface, either by thermal conduction or by nonthermal electrons accelerated at the shock front.

Acknowledgements. He I data were provided by the High Altitude Observatory of the National Center for Atmospheric Research, which is sponsored by the National Science Foundation, and we thank T. Holzer, H. Gilbert and A. Stanger for their support. Hα data is used with permission of BBSO, New Jersey Institute of Technology, and we thank the BBSO staff for their kind support. A. W. and A. H. acknowledge the support of the Austrian FWF Project P13653-PHY. B. V. is grateful to the colleagues from the Institute for Geophysics, Astrophysic and Meteorology for their hospitality during his stay in Graz and acknowledges the financial support of the University of Graz. The authors are thankful to the referee for very constructive comments and suggestions.

References

Andretta, V., & Jones, H. P. 1997, ApJ, 489, 375
Benz, A. O. 1993, Plasma Astrophysics (Kluwer, Dordrecht)
Bougeret, J.-L., Kaiser, M. L., Kellogg, P. J., et al. 1995, Space Sci. Rev., 71, 231
Brajša, R., Pohjolainen, S., Ruždjak, V., et al. 1996, Sol. Phys., 163, 79
Brueckner, G. E., Howard, R. A., Koomen, M. J., et al. 1995, Sol. Phys., 162, 357
Delaboudinière, J.-P., Artzner, G. E., Brunaud, J., et al. 1995, Sol. Phys., 162, 291
Delannée, C., & Aulanier, G. 1999, Sol. Phys., 190, 107
Denker, C., Johannesson, A., Marquette, W., et al. 1999, Sol. Phys., 184, 87
Dodson, H. W., & Hedeman, R. E. 1968, Sol. Phys., 4, 229
Eto, S., Isobe, H., Narukage, N., et al. 2002, Publ. Astron. Soc. Jpn, 54, 481
Fisher, R. R., Lee, R. H., MacQueen, R. M., & Poland, A. I. 1981, Appl. Opt., 20, 1094
Gary, G. A. 2001, Sol. Phys. 203, 71
Giovanelli, R. G., Hall, D. N. B., & Harvey, J. W., 1972, Sol. Phys., 22, 53
Jones, H. P., Duvall,T. L., Jr., Harvey, J. W., et al. 1992, Sol. Phys., 139, 211
Khan, J. I., & Aurass, H. 2002, A&A, 383, 1018
Klassen, A., Aurass, H., Mann, G., & Thompson, B. J. 2000, A&AS, 141, 357
Landau, L. D., & Lifshitz, E. M. 1987, Fluid Mechanics, 2d ed. (Oxford: Pergamon Press)

[5] For details of the formation mechanism see Vršnak & Lulić (2000a,b); for the decay of simple waves see Landau & Lifshitz (1987).

MacQueen, R. M., Blankner, J. G., Elmore, D. F., Lecinski, A. R., & White, O. R. 1998, Sol. Phys., 182, 97
Manheimer, W. M., Klein, H. H. 1975, Phys. Fluids, 18, 1299
Mann, G., Classen, T., & Aurass, H. 1994, A&A, 295, 775
Mann, G., Aurass, H., Klassen, A., Estel, C., & Thompson, B. J. 1999, in Proc. 8th SOHO Workshop on Plasma Dynamics and Diagnostics in Transition Region & Corona, ed. B. Kaldeich-Schürmann (SP-446) (Noordwijk: ESA), 477
Mann, G., Klassen, A., Aurass, H., & Classen, H.-T. 2002, A&A, submitted
Manoharan, P. K., van Driel-Gesztelyi, L., Pick, M., & Démoulin, P. 1996, ApJ, 468, L73
McDonald, L., Harra-Murnion, L. K., & Culhane, J. L. 1999, Sol. Phys., 185, 323
Moreton, G. E., & Ramsey, H. E. 1960, PASP, 72, 357
Narukage, N., Hudson, H. S., Morimoto, T., Akiyama, S., Kitai, R., Kurokawa, H., & Shibata, K. 2002, ApJ, 572, L109
Nelson, G. S., & Melrose, D. B. 1985, in Solar Radiophysics, ed. D. J. McLean, & N. R. Labrum (Cambridge Univ. Press, Cambridge), 333
Smith, S. F., & Harvey, K. L. 1971, in Physics of the Solar Corona, ed. C. J. Macris (Dordrecht: Reidel Publ. Co.), 156
Rust, D. M., & Somov, B. V. 1984, Sol. Phys., 93, 95
Stewart, R. T., & Magun, A. 1980, Proc. ASA, 4, 53
Thompson, B. J., et al. 1998, Geophys. Res. Lett., 25, 2465
Thompson, B. J., et al. 1999, ApJ, 517, L151
Thompson, B. J., et al. 2000, Sol. Phys., 193, 161
Uchida, Y. 1968, Sol. Phys., 4, 30
Uchida, Y., Altschuler, M. D., & Newkirk, G., Jr. 1973, Sol. Phys., 28, 495
Uchida, Y. 1974, Sol. Phys., 39, 431
Vršnak, B., & Lulić., S. 2000a, Sol. Phys., 196, 157
Vršnak, B., & Lulić., S. 2000b, Sol. Phys., 196, 181
Vršnak, B., Warmuth, A., Maričić, D., Otruba, W., & Ruždjak, V. 2002, A&A, submitted
Vršnak, B., Aurass, H., Magdalenić, J., & Gopalswamy, N. 2001, A&A, 377, 321
Warmuth, A., Vršnak, B., Aurass, H., & Hanslmeier, A. 2001, ApJ, 560, L105
Warmuth, A., Vršnak, B., Aurass, H., & Hanslmeier, A. 2002, in Proc. SOLSPA 2001 Euroconference, in press
Wu, S. T., Zheng, H., Wang, S., et al. 2001, J. Geophys. Res., 106, 25 089
Wang, Y.-M. 2000, ApJ, 543, L89